Supplementary materials for:

Synchronous Reduction-Oxidation Process for Efficient Removal of Trichloroacetic Acid: H* Initiates Dechlorination and •OH Is Responsible for Removal Efficiency

Jun Zhang,[a] Qinghua Ji,[a] Huachun Lan,[a] Gong Zhang,[a] Huijuan Liu,[a] Jiuhui Qu,[a,b]*

a, Center for Water and Ecology, State Key Joint Laboratory of Environment Simulation and Pollution Control, School of Environment, Tsinghua University, Beijing 100084, China

b, Key Laboratory of Drinking Water Science and Technology, Research Center for Eco-Environmental Sciences, Chinese Academy of Sciences, Beijing 100085, China

* Corresponding Author.

(G. Zhang) Phone/Fax: +86-10-62790565; E-mail: gongzhang@mail.tsinghua.edu.cn.

This part includes:

5 Texts

3 Schemes

17 Figures

Density Functional Theory (DFT) Calculation. For CuO/Pd systems, the CuO surface was built, the bottom three atomic layers were fixed and the three atomic layers were relaxed. Moreover, a Pd cluster (Pd_{12}) was loaded on the CuO surface for CuO/Pd system. For reactions, the intermediates were adsorbed on the surfaces of CuO and CuO/Pd. For CCl_3−COOH systems, the structural optimization and electronic structures have been calculated using DMol3 code. The generalized gradient approximation (GGA) with the Perdew-Burke-Ernzerhof (PBE) functional and all-electron double numerical basis set with polarized function (DNP) have been employed. The convergence tolerance of energy, maximum force and maximum displacement were 1.0×10^{-5} Ha, 2.0×10^{-3} Ha/Å and 5.0×10^{-3} Å (1 Ha = 27.21 eV) for geometry optimization. The Grimme method for DFT-D correction was considered for all calculations. Each atom in the storage models was allowed to relax to the minimum in the enthalpy without any constraints.

Adsorption energy ΔE of A group on the surface of substrates was defined as:

$$\Delta E = E_{*\mathrm{A}} - (E_{*} + E_{\mathrm{A}})$$

where *A and * denote the adsorption of A group on substrates and the bare substrates, E_{A} denotes the energy of A group.

Gibbs free energy change (ΔG) of each chemical reaction is calculated by:

$$\Delta G = \Delta E + \Delta ZPE - T\Delta S + \Delta G_{\mathrm{U}}$$

where E, ZPE, T and S denote the calculated total energy, zero-point energy, temperature and entropy, respectively. $\Delta G_{\mathrm{U}} = -\mathrm{e}U$ (U was the potential measured against normal hydrogen electrode). Here, T = 300K was considered.

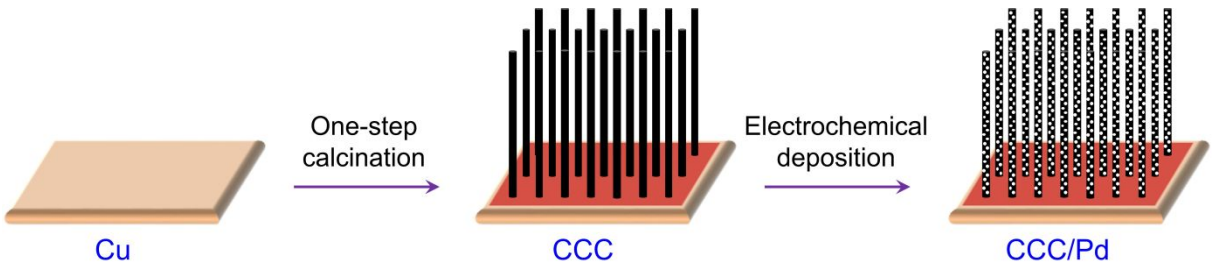

Scheme S1. Schematic of CCC and CCC/Pd photoelectrode synthesis.

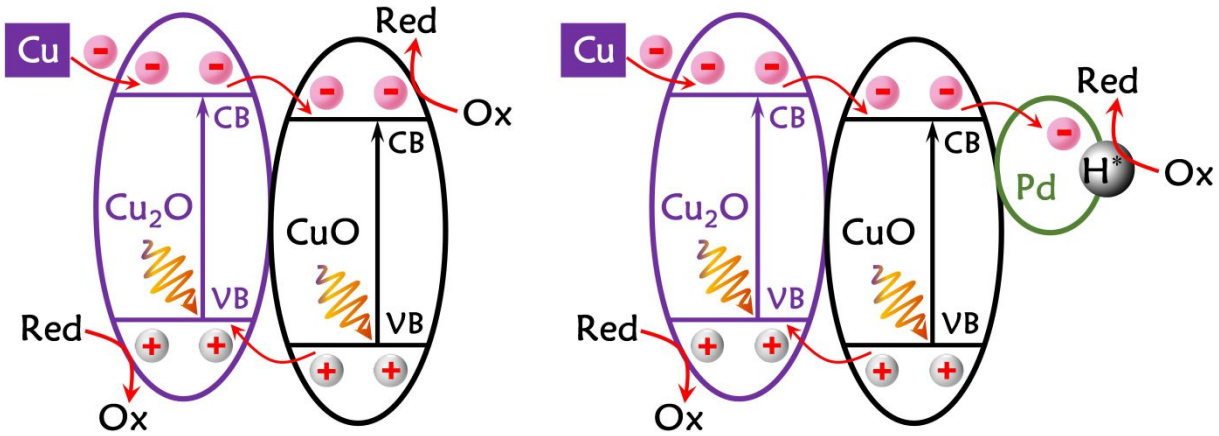

Scheme S2. Schematic of charge transfer and redox existed in CCC and CCC/Pd photoelectrode in visible light.

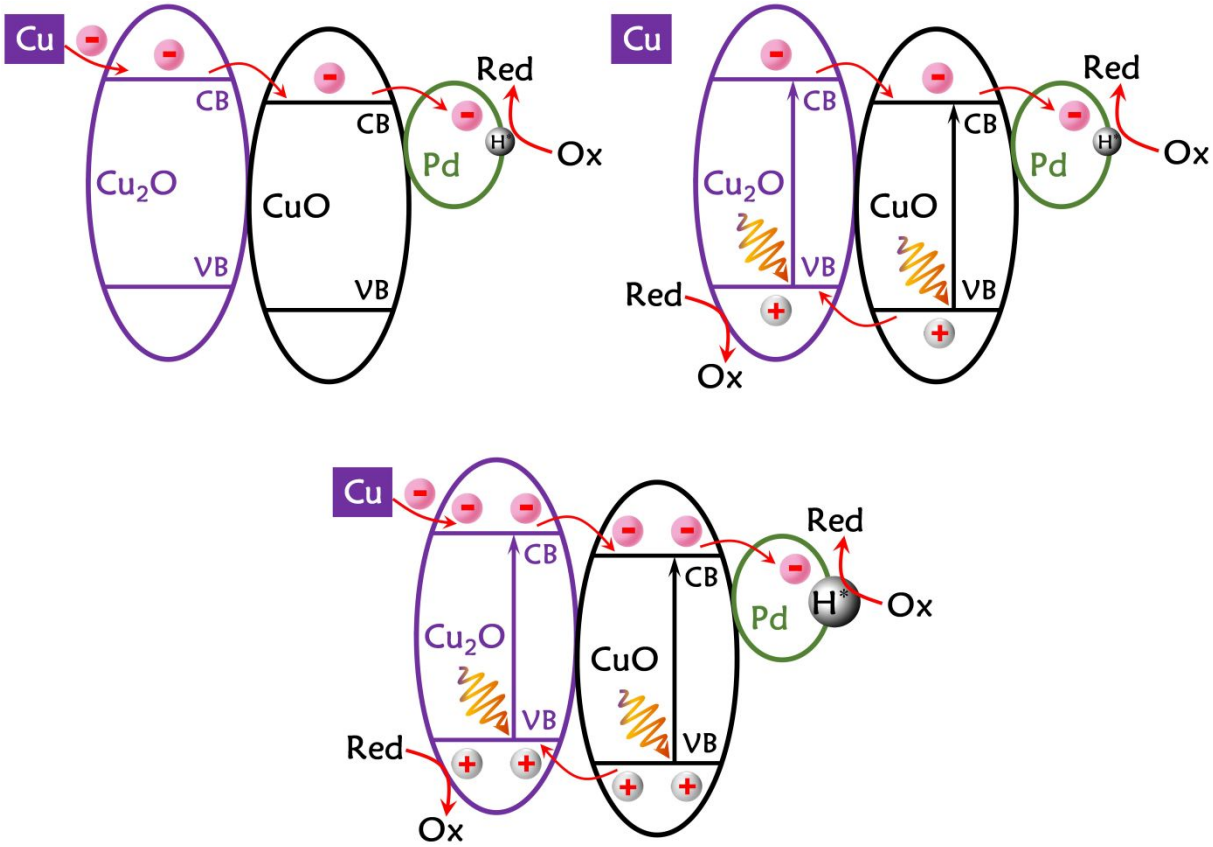

Scheme S3. Schematic of charge transfer and redox in electrocatalysis, photocatalysis and photoelectrocatalysis of CCC/Pd photoelectrode.

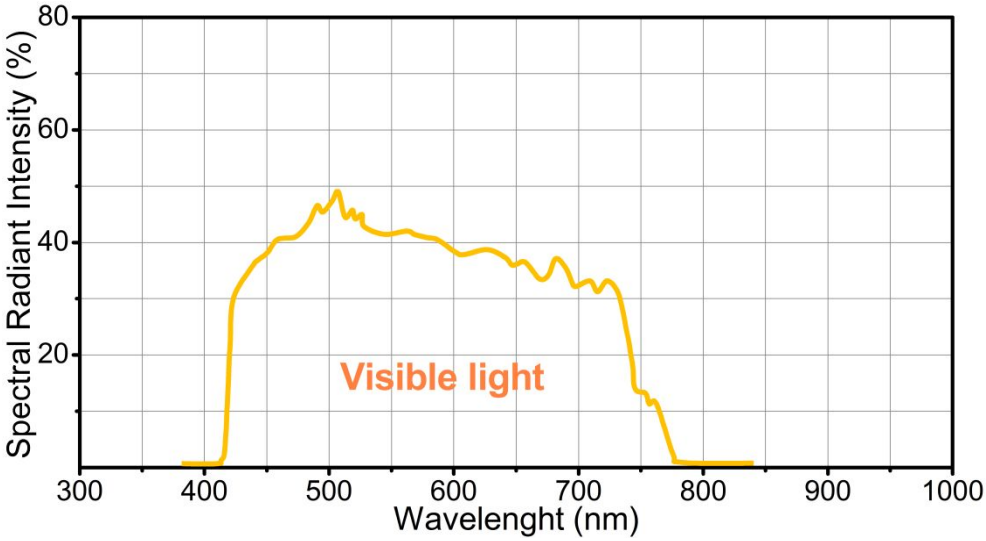

Figure S1. Visible light wavelength spectrum of the Xenon lamp used in the research.

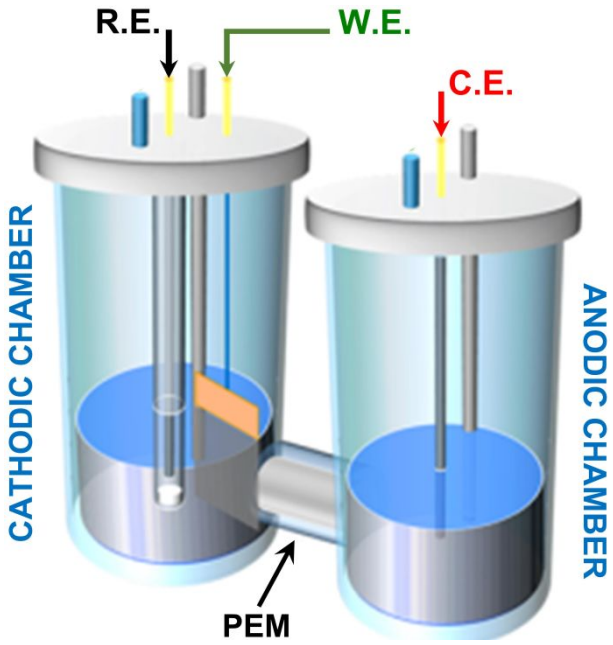

Figure S2. Schematic of double-chamber electrolysis cell used in this study.

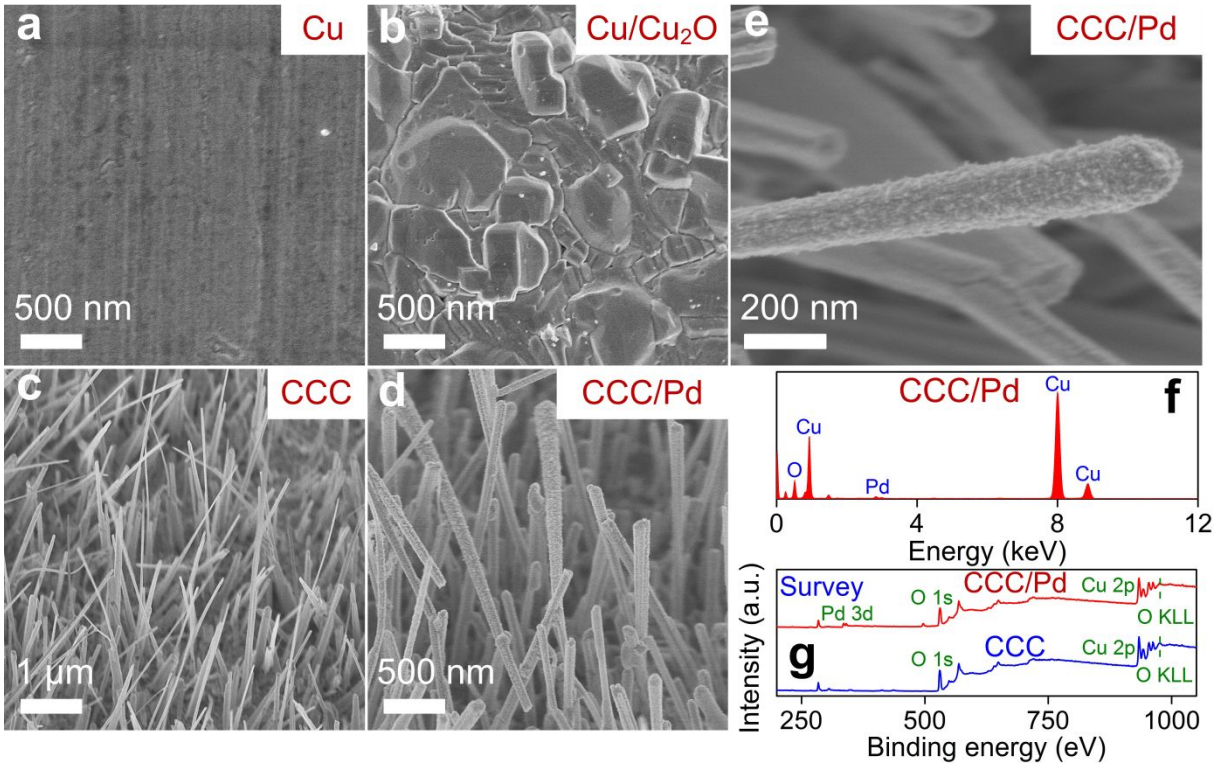

Figure S3. SEM images (a−e), EDX spectrum (f) and XPS survey spectrum (g) of as-prepared Cu, Cu/Cu_2O, CCC and CCC/Pd electrode.

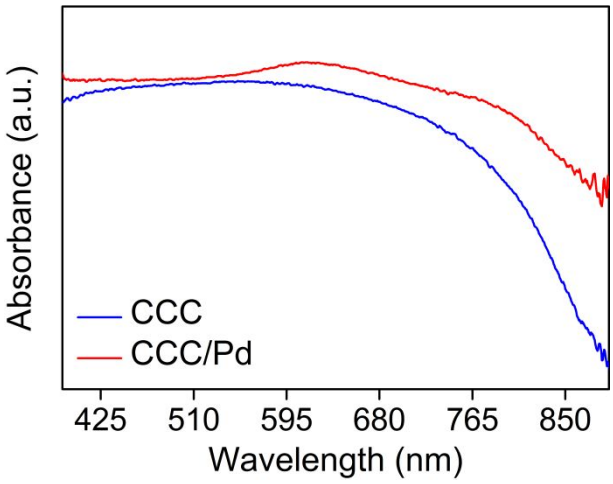

Figure S4. UV-DRS spectra of CCC and CCC/Pd photocathodes.

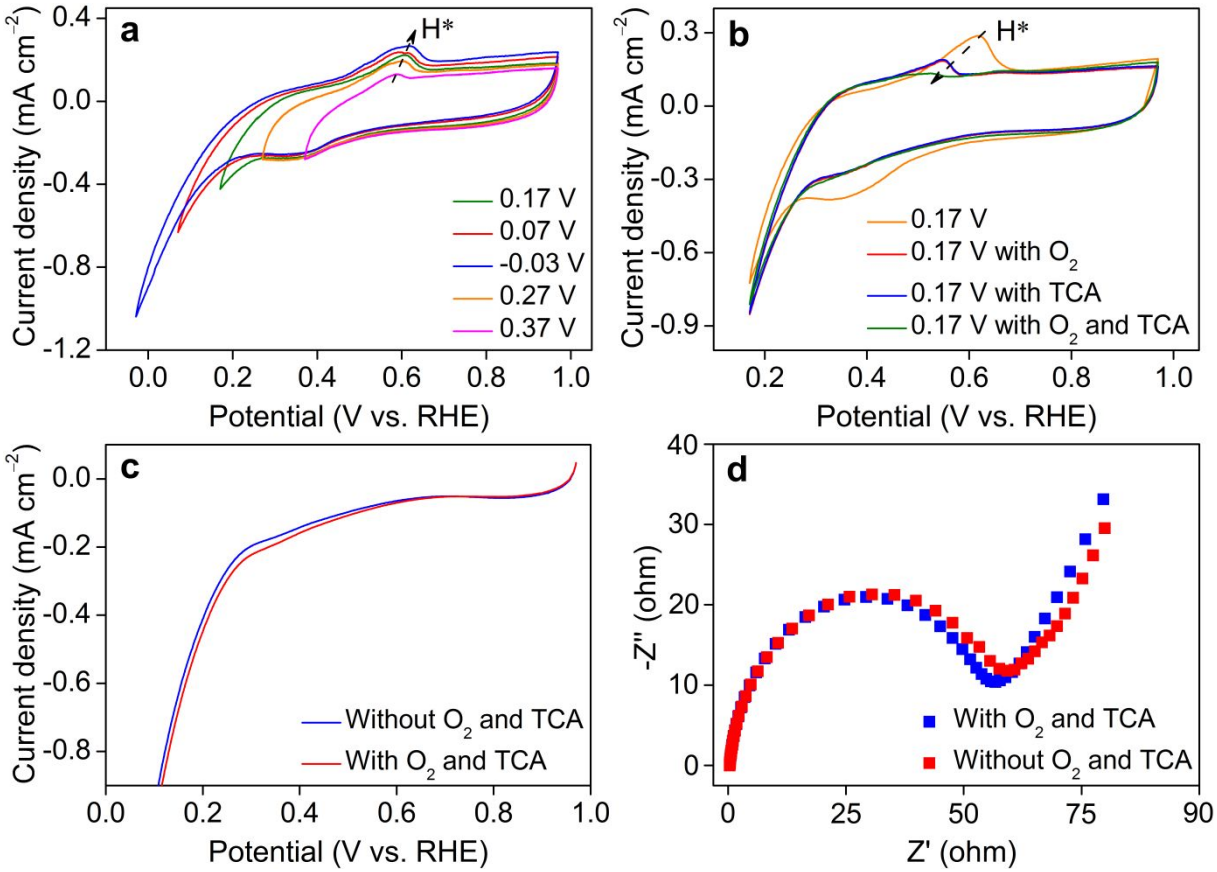

Figure S5. CV curves of the CCC/Pd in N_2-saturated condition with different CV starting potentials (a); CV (b), LSV (c) and EIS (d) curves of the CCC/Pd in N_2-saturated condition with or/and without O_2 and TCA. Experimental condition: temperature (25 °C), electrolyte (50 mM Na_2SO_4), CV and LSV scan rate = 10 mV s^{-1}, applied voltage (−0.5 V vs. RHE), frequency range (0.1 Hz−100 kHz), disturbance voltage (10mV), in visible light irradiation.

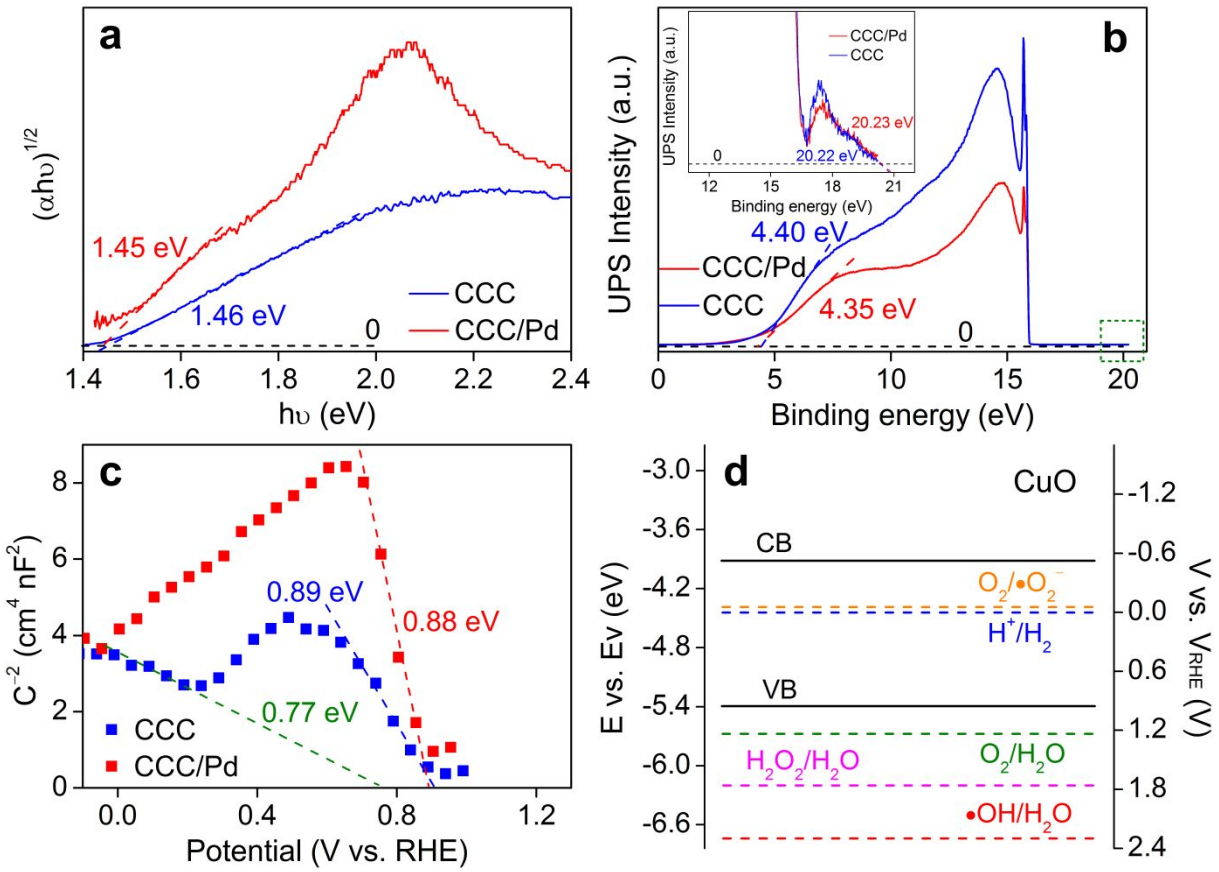

Figure S6 Band gap values (a), UPS spectra (b), and Mott-schottky curves (c) Band structure diagram (d) for CCC and CCC/Pd. Experimental condition: temperature (25 °C), electrolyte (50 mM Na_2SO_4), scan rate = 10 mV s^{-1}, applied voltage (−0.5 V vs. RHE), frequency range (5 kHz), in visible light irradiation.

The analyses of band structures of CCC and CCC/Pd was conductive to reveal the pathway and mechanism of •OH generation (Figure S6). The band gaps (E_g) of CCC and CCC/Pd were calculated by Tauc plots, with the E_g values at 1.46 and 1.45 eV, respectively. UPS spectra were used to determine the VB energy (E_v) of CCC (5.4 eV) and CCC/Pd (5.34 eV) via subtracting the width of the He I UPS spectra from the excitation energy (21.22 eV). The CB gaps (E_c) were thus estimated at 3.94 eV (CCC) and 3.89 eV (CCC/Pd) through $E_v - E_g$. The values of E_c, E_v and E_g had be converted from in electron volts to electrochemical energy potentials (volts) according to the reference standard (0 V versus RHE equaled −4.44 eV versus evac). Mott-Schottky plots had

measured the flat band potential (V_{fb}) of CCC (0.89 eV) and CCC/Pd (0.88 eV), which was in good agreement with above analyses and further revealed the band structures of CCC and CCC/Pd.

Both CCC/Pd and CCC photocathodes had the appropriate CB position, far more positive than the standard reduction potential of $O_2/{\bullet}O_2^-$ (−0.146 V (vs. RHE)), meaning that the $\bullet O_2^-$ could generated smoothly on the surface of CCC/Pd and CCC (Figure S6d). ESR spectra analyses further confirmed this view by having captured the characteristic signal of DMPO−$\bullet O_2^-$ (Figure S8b). It was worth noting that the signal intensity of $\bullet O_2^-$ had relatively decreased after loading Pd to CCC, which was mainly attributed to the fast electron transfer between CCC and Pd. Abundant electrons gathered in Pd and produced H* continuously. The standard redox potential of $\bullet OH/OH^-$ was 2.3 eV (vs. RHE) which was more positive than the VB position of CCC/Pd and CCC. Thus, the •OH could not be formed in thermodynamics on the surface of CCC/Pd and CCC. However, it was not consistent with the ESR analyses results. Thus, the •OH existed in CCC/Pd and CCC photoelectrocatalytic systems must be generated by other means.

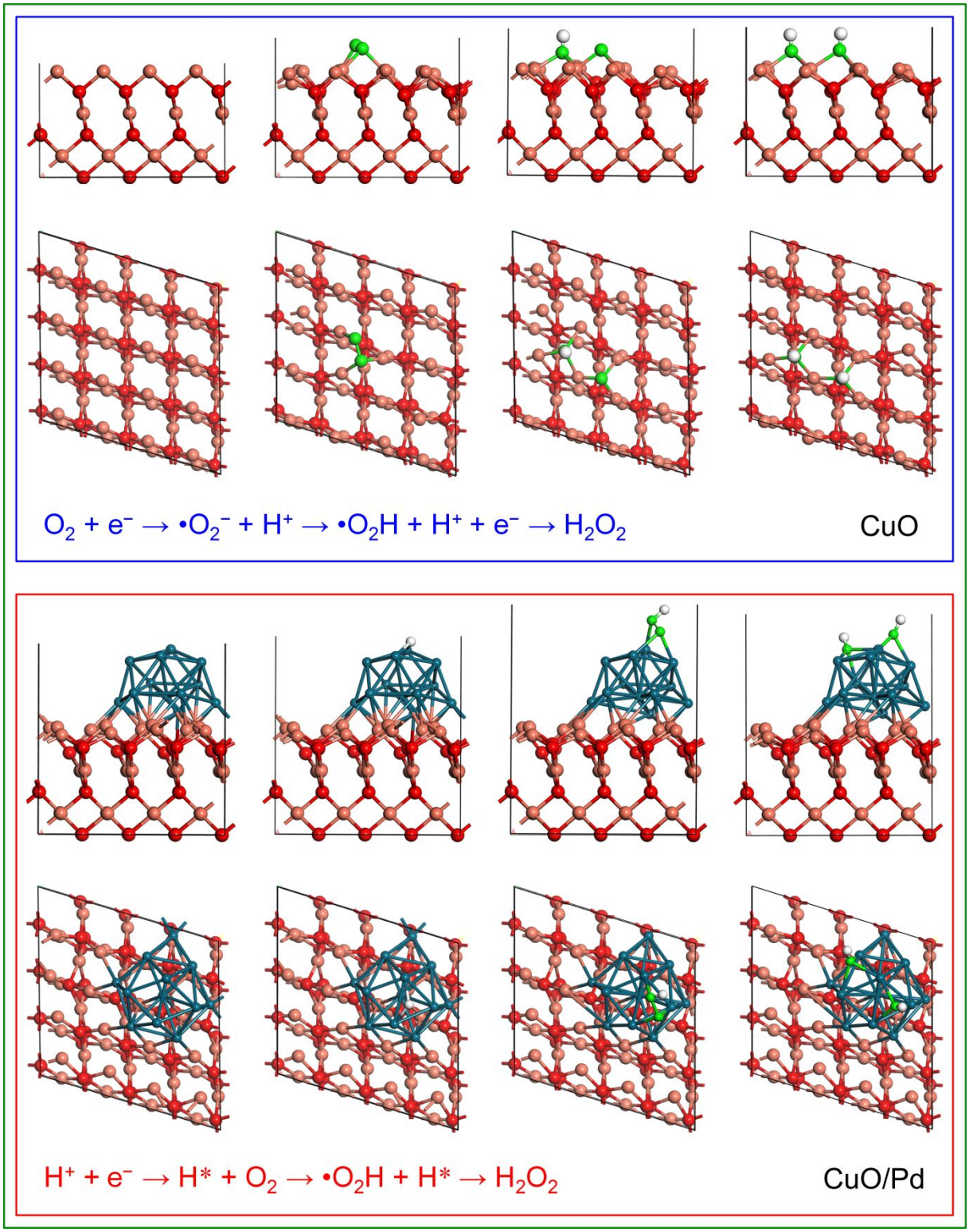

Figure S7. Top and side views of the H*, $\bullet O_2^-$, $HO_2\bullet$ and H_2O_2 formation processes on CuO(001) and CuO(001)/Pd, respectively.

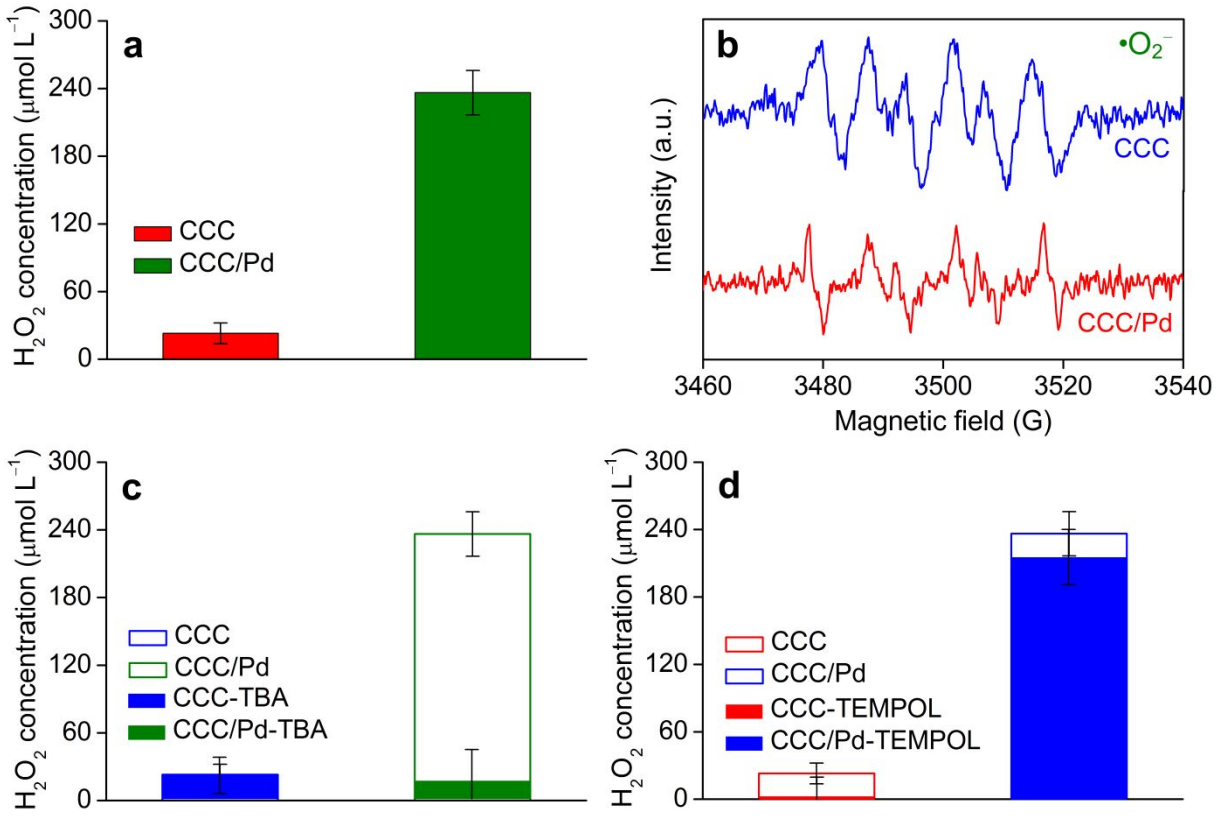

Figure S8. Generated H_2O_2 contents of the CCC and CCC/Pd (a); DMPO spin-trapping ESR spectra recorded with CCC and CCC/Pd in methanol solution (b); Generated H_2O_2 contents of the CCC and CCC/Pd with or without TBA (c) and TEMPOL (d). Conditions: electrolyte (5 mM Na_2SO_4), reaction time (60 min), photocathode potential (−0.5 V vs. RHE), temperature (25 °C), in visible light irradiation.

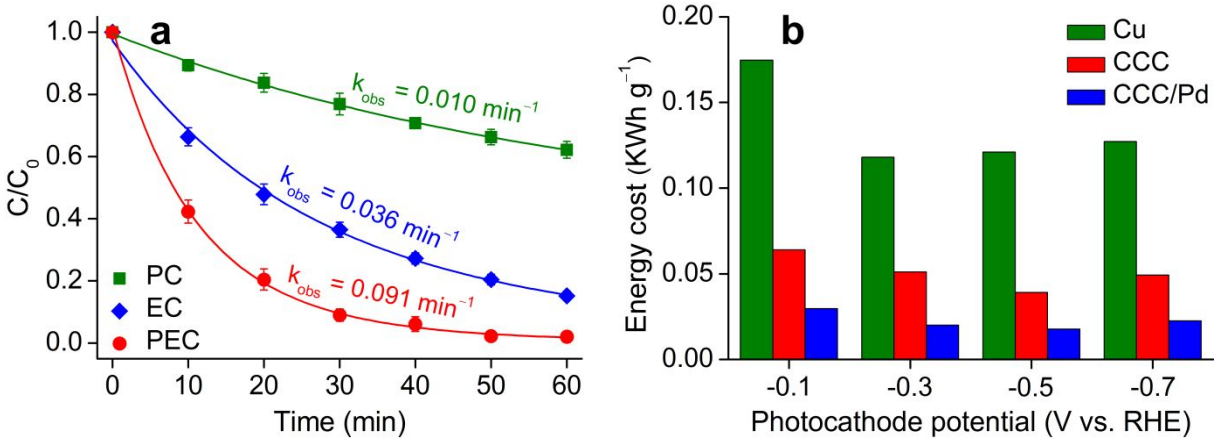

Figure S9. Reaction kinetics fitting of PC, EC and PEC systems (a); Energy cost of as-prepared cathodes at different voltages (b). Experimental condition: TCA_0 (5 mg L^{-1}), electrolyte (5 mM Na_2SO_4), initial pH (5.1), reaction time (60 min), photocathode potential (−0.5 V vs. RHE), temperature (25 °C), in visible light irradiation.

Energy consumption was an extremely important parameter in process of actual water treatment, which could be calculated by $E = 10^{-3} \times UItm^{-1}$, where U = potential (V), I = current (A), t = reaction time (h), and m = dechlorinated TCA mass (g). While decreasing potentials from 0.0 to −0.7 V, the CCC/Pd photoelectrode always possessed the lowest energy cost compared to Cu and CCC (Figure S9b). Such superior performance was mainly due to the synergism of Pd and CCC.

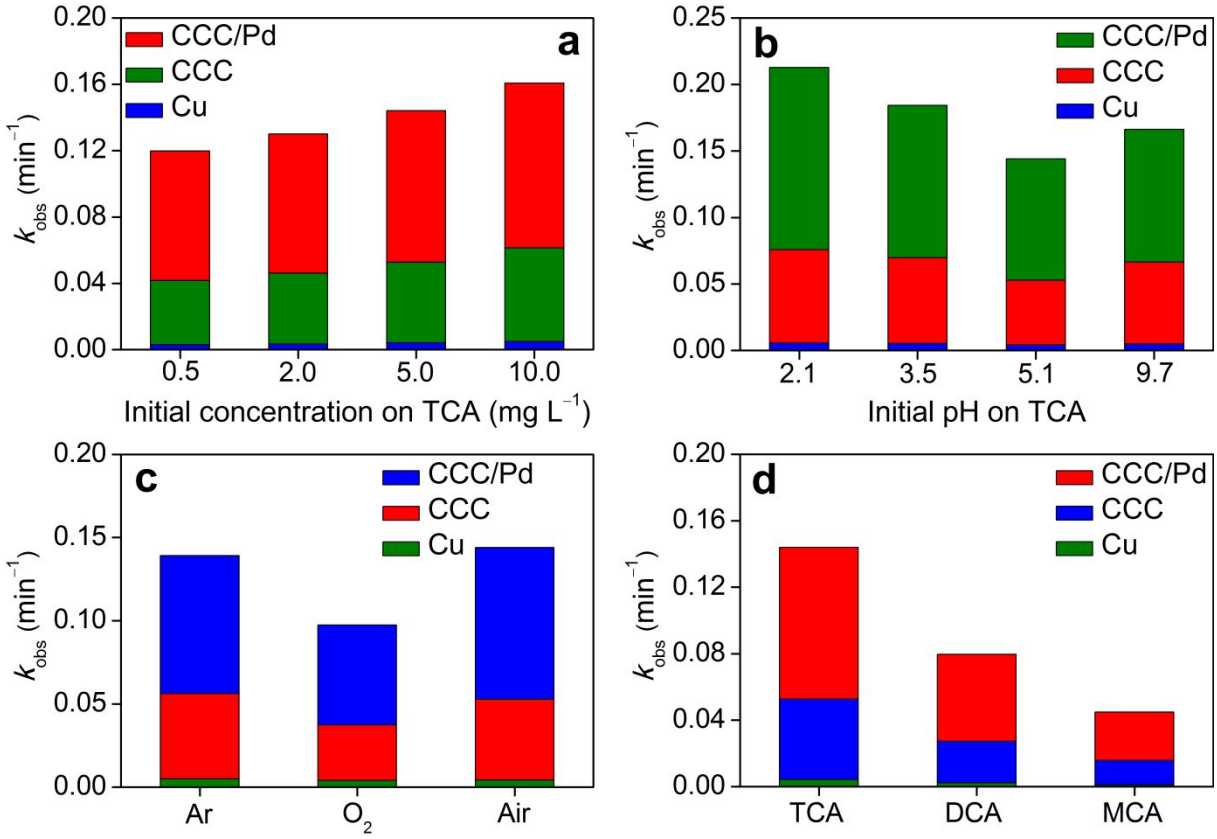

Figure S10. The k_{obs} of TCA removal in different initial TCA concentration (a) and initial pH on TCA (b); Effect of dissolved oxygen on TCA removal (c); The k_{obs} of TCA, DCA and MCA removal for as-prepared electrodes (d); Experimental condition: photocathode potential (−0.5 V vs. RHE), electrolyte (5 mM Na_2SO_4), reaction time (60 min), temperature (25 °C), in visible light irradiation.

For as-prepared electrodes, the dechloridation rates of TCA were higher than that of DCA and MCA in the same conditions (Figure S10d). The rule was that the less chlorine was more difficult to dechlorinate, which was likely caused by the stable structure for MCA and DCA. The *J-V* analysis showed that there were no electrons transferred from CCC/Pd to TCA, DCA and MCA (Figure S11d). This further confirmed that the dechlorination of CAs by CCC/Pd was through the compound reaction via the full cooperation of H* and •OH but not direct electron transfer. That was, the electrons in CCC/Pd would combine with H^+ to generate H*, and then

reduced CAs instead of the direct electron transfer between CCC/Pd and CAs.

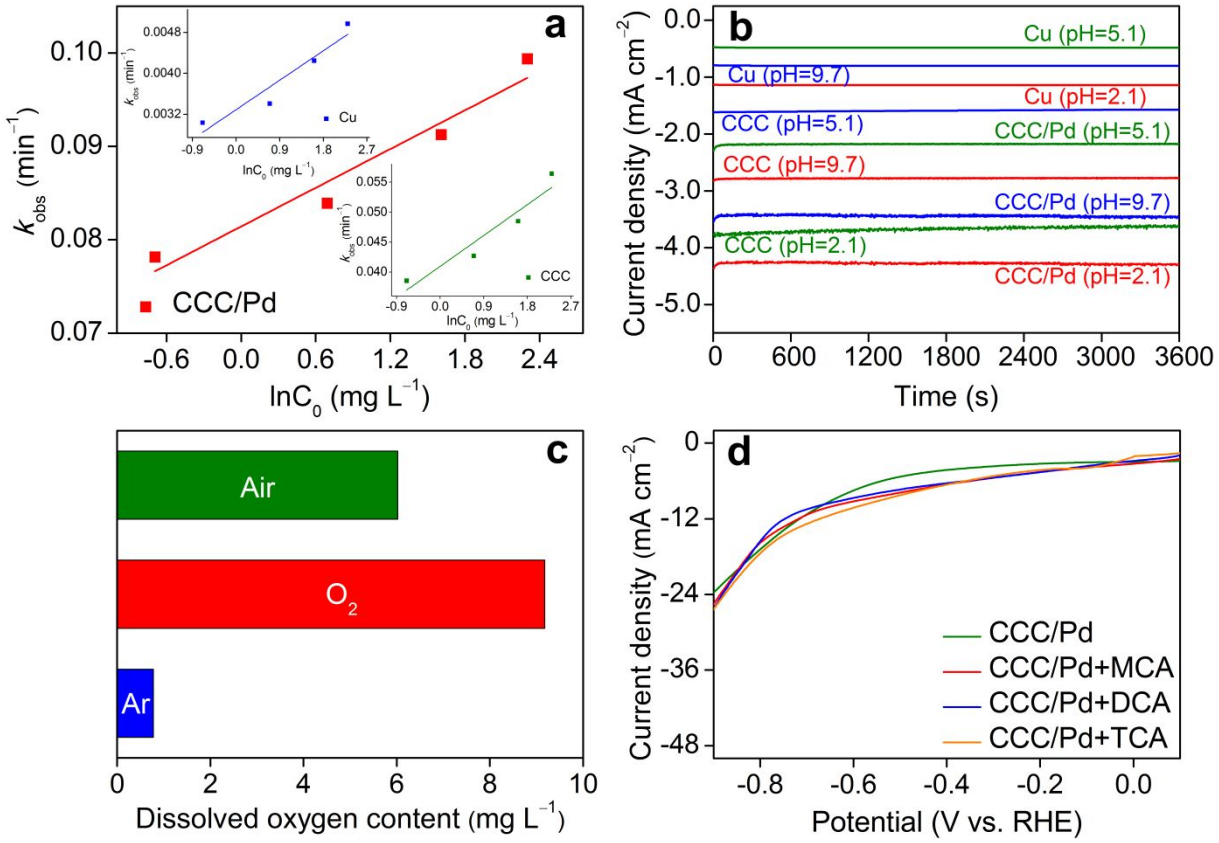

Figure S11. The relationship between k_{obs} and logarithm of initial TCA concentration (a); Current density in different initial TCA pH for as-prepared electrodes (b); Dissolved oxygen content in different conditions (c); LSV curves of CCC/Pd in the presence of TCA, DCA and MCA (d). Experimental condition: applied voltage (−0.5 V vs. RHE), temperature (25 °C), electrolyte (5 mM Na_2SO_4), LSV scan rate = 10 mV s^{-1}, in visible light irradiation.

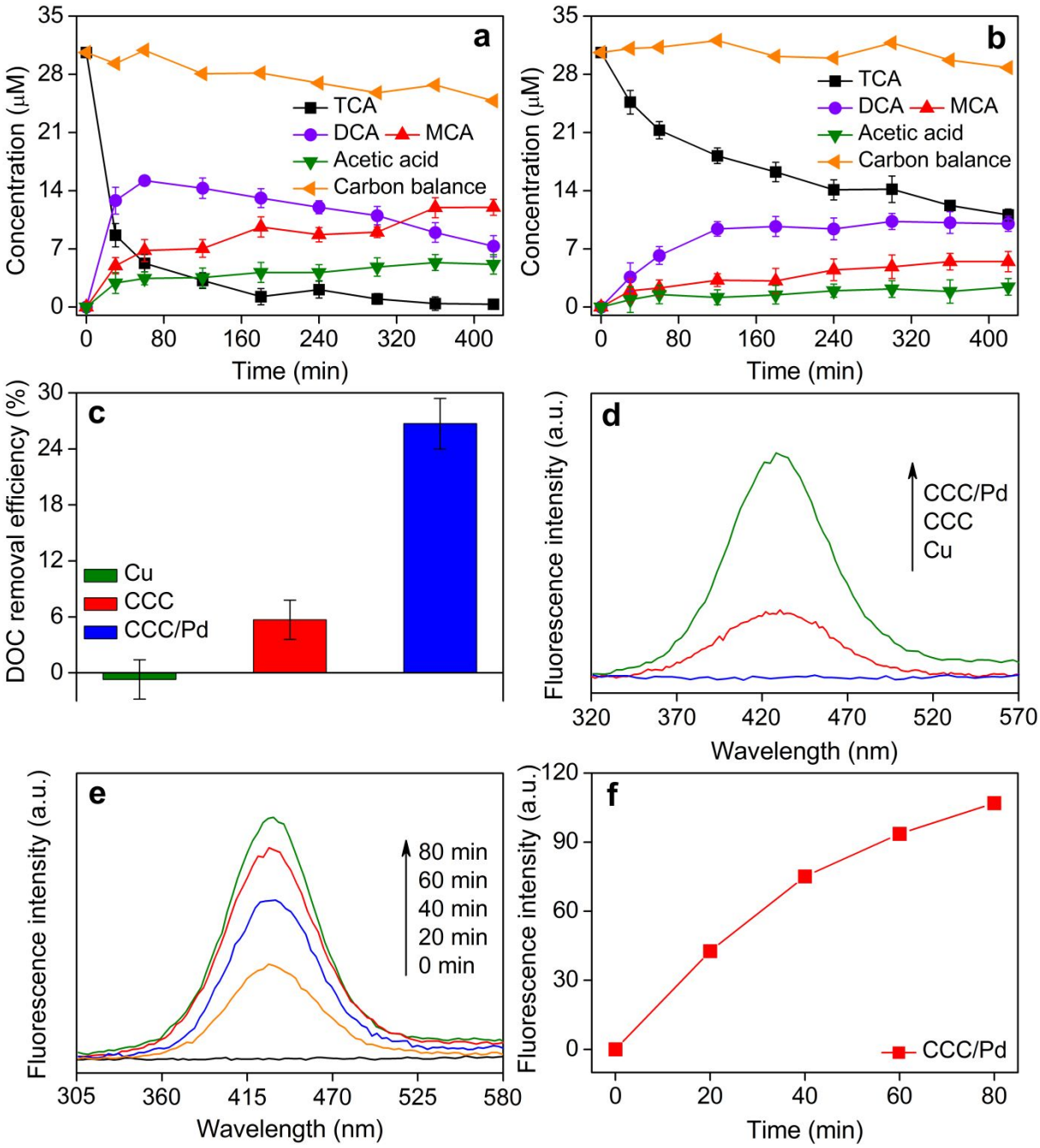

Figure S12. Intermediates, final products and carbon balance of TCA removal for CCC (a) and Cu (b); DOC removal efficiency of TCA removal for as-prepared electrodes (c); PL intensity for as-prepared electrodes (d); PL intensity for CCC/Pd at different reaction time (e and f). Experimental condition: TCA_0 (5 mg L^{-1}), applied voltage (−0.5 V vs. RHE), temperature (25 °C), electrolyte (5 mM Na_2SO_4), in visible light irradiation.

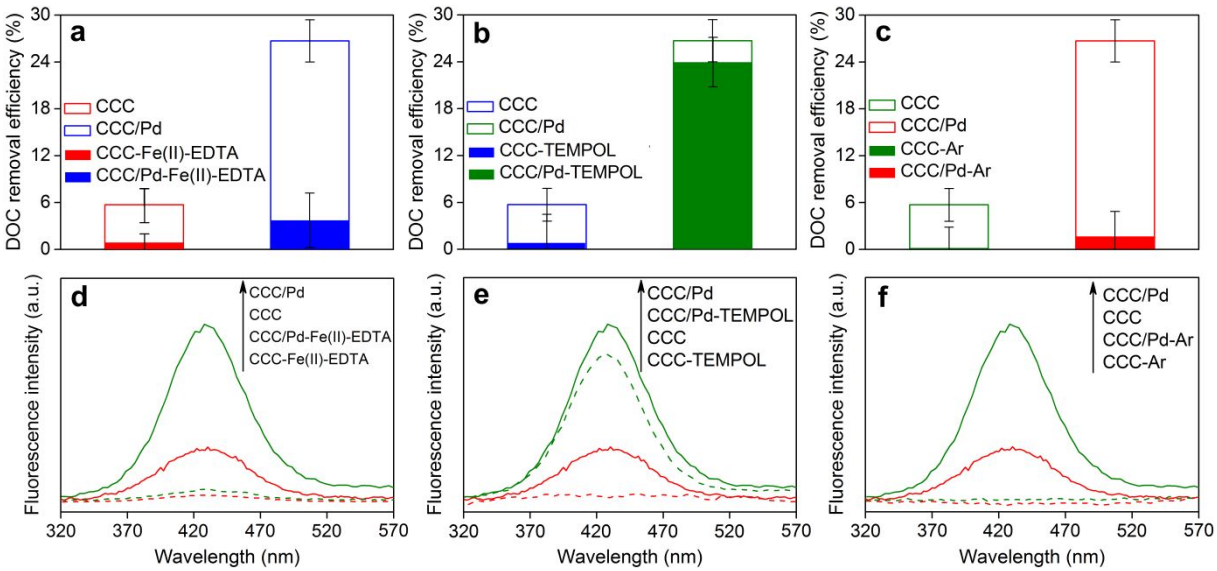

Figure S13. DOC removal efficiency and corresponding PL intensity with or without addition of Fe(II)-EDTA (a and d), TEMPOL (b and e) and Ar (c and f) for CCC and CCC/Pd photoelectrodes. Conditions: TCA_0 (5 mg L^{-1}), electrolyte (5 mM Na_2SO_4), initial pH (5.1), reaction time (60 min), photocathode potential (−0.5 V vs. RHE), temperature (25 °C), in visible light irradiation.

In order to reveal the effect of H_2O_2, the scavenger-quenching experiments were performed to compare DOC removal efficiency (Figure S13a). It was clearly that the mineralization efficiency and PL intensity (•OH) radically reduced both in CCC/Pd and CCC systems with presence of Fe(II)-EDTA, which accurately verified the above guesses (Figure S13a and S13d). The generated H_2O_2 content could be detected and showed in Figure S8a, and the large gap of H_2O_2 concentration was corresponding to the discrepant amount of generated •OH. And then we needed to determine the synthetic route of H_2O_2 in CCC/Pd and CCC systems, respectively. After quenching the $•O_2^-$ by TEMPOL, the mineralization efficiency and PL intensity (•OH) almost completely disappeared in CCC system, but only a slight decline of DOC and PL appeared in CCC/Pd system (Figure S13b and S13e). When cleared out the dissolved oxygen in CCC/Pd and

CCC systems, both mineralization efficiency and PL intensity (•OH) were sharply decreased (Figure S13c and S13f). This indicated that the •OH generated in CCC system was all come from the conversion of O_2 by way of $O_2 \rightarrow \bullet O_2^- \rightarrow H_2O_2 \rightarrow \bullet OH$. And the process of $O_2 \rightarrow HO_2\bullet \rightarrow H_2O_2 \rightarrow \bullet OH$ were identified as the main pathway of •OH generation in CCC/Pd system. We also detected the H_2O_2 content in CCC/Pd and CCC systems when using TBA (for H* and $HO_2\bullet$) and TEMPOL (for $\bullet O_2^-$) as quenchers, respectively, which was in agreement with above analyses (Figure S8c and S8d). The H* and e^- played the key roles in the process of •OH generation at CCC/Pd and CCC, respectively (Scheme S2). The results further confirmed the correctness of our inference.

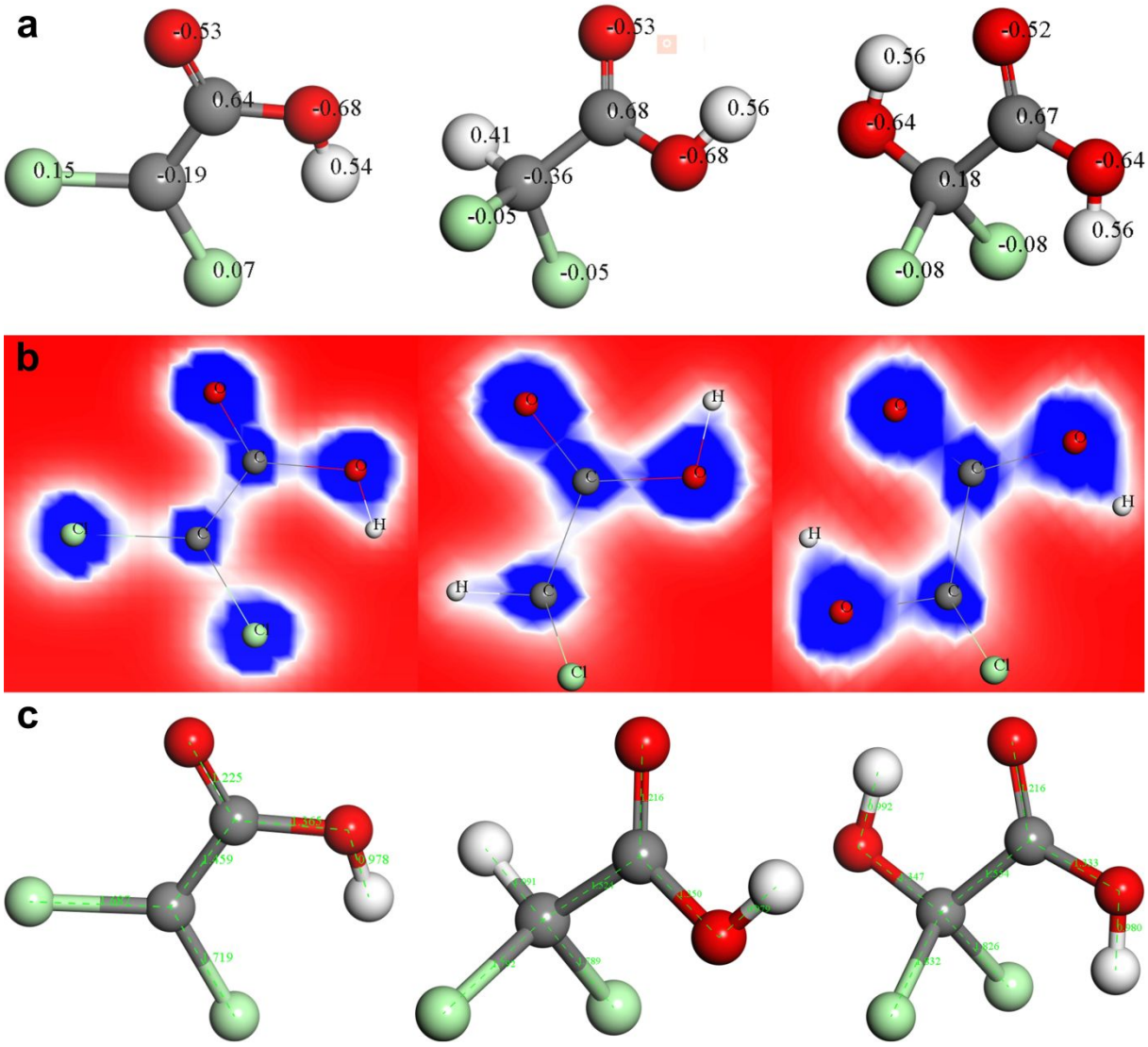

Figure S14. Electron density of atoms existing in $Cl_2C{-}COOH$, $HCl_2C{-}COOH$ and $HOCl_2C{-}COOH$ (a); Two-dimensional valence-electron density color-filled maps of $Cl_2C{-}COOH$, $HCl_2C{-}COOH$ and $HOCl_2C{-}COOH$ (b); Bond length in $Cl_2C{-}COOH$, $HCl_2C{-}COOH$ and $HOCl_2C{-}COOH$ (c).

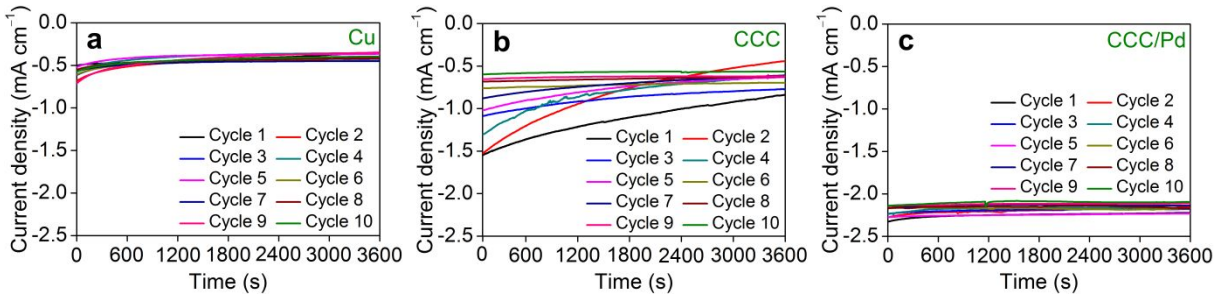

Figure S15. The corresponding chronoamperometric currents for ten times repeated tests of Cu, CCC and CCC/Pd electrodes for TCA removal, respectively. Experimental condition: TCA_0 (5 mg L^{-1}), electrolyte (5 mM Na_2SO_4), initial pH (5.1), each test reaction time (60 min), photocathode potential (−0.5 V vs. RHE), temperature (25 °C), LSV scan rate = 10 mV s^{-1}, in visible light irradiation.

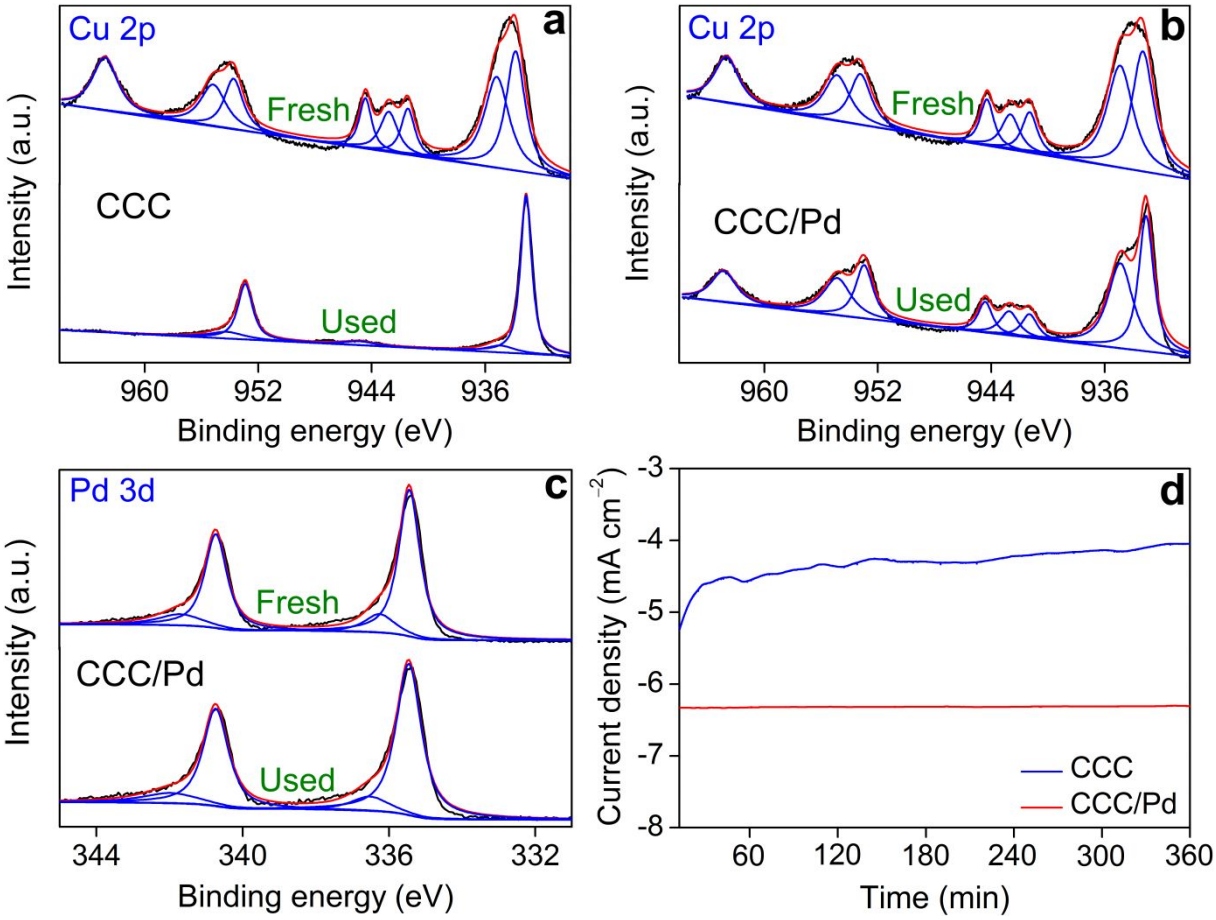

Figure S16. High-resolution XPS spectra of fresh and used as-prepared photoelectrodes. Experimental condition: temperature (25 °C), electrolyte (50 mM Na_2SO_4), applied voltage (−0.5 V vs. RHE), in visible light irradiation.

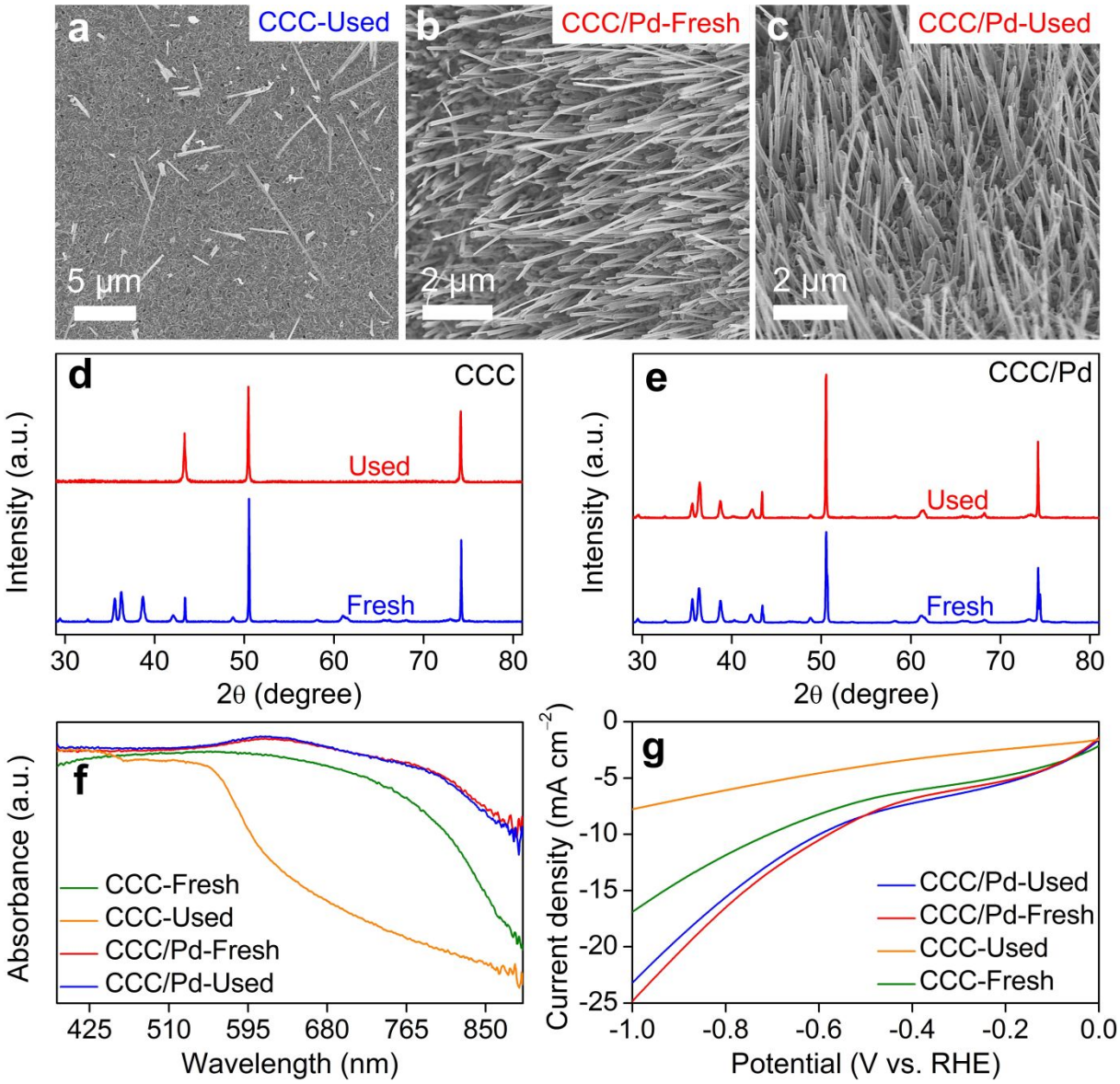

Figure S17. The SEM, XRD, DRS and LSV analyses of fresh and used as-prepared photoelectrodes. Experimental condition: temperature (25 °C), electrolyte (50 mM Na_2SO_4), LSV scan rate = 10 mV s^{-1}, in visible light irradiation.